Materials Reports: Energy 6 (2026) 100431

Contents lists available at ScienceDirect

Materials Reports: Energy

journal homepage: www.keaipublishing.com/en/journals/materials-reports-energy

Original Research Report

# Cobalt-atom electrocatalytic framework on $CO_2$-derived defective carbon for enhanced $H_2O_2$ production across pH levels

Jimin Lee[a,1], Yeongjun Yoon[b,1], Wenjun Zhang[c,1], Won Chan Yun[a,1], Keun Hwa Chae[d], Ayeong Byeon[e], Jinli Qiao[f,g], Jong Min Kim[c,h,*], Kyeounghak Kim[b,**], Jae W. Lee[a,***]

[a] Department of Chemical and Biomolecular Engineering, Korea Advanced Institute of Science and Technology, Daejeon, 34141, Republic of Korea
[b] Department of Chemical Engineering, Hanyang University, Seoul, 04763, Republic of Korea
[c] Extreme Materials Research Center, Korea Institute of Science and Technology, Seoul, 02792, Republic of Korea
[d] Advanced Analysis Data Center, Korea Institute of Science and Technology (KIST), Seoul, 02792, Republic of Korea
[e] Department of Chemical Engineering, Chungbuk National University, Cheongju, 28644, Republic of Korea
[f] State Key Laboratory of Advanced Fiber Materials, College of Environmental Science and Engineering, Donghua University, Shanghai, 201620, China
[g] Shanghai Institute of Pollution Control and Ecological Security, Shanghai, 200092, China
[h] KHU-KIST Department of Converging Science and Technology, Kyung Hee University, Seoul, 02447, Republic of Korea

ARTICLE INFO

*Keywords:*
Oxygen reduction reaction
Hydrogen peroxide production
Single-atom catalysts
Defective carbon
Carbon dioxide conversion

ABSTRACT

The increasing demand for hydrogen peroxide ($H_2O_2$) has highlighted the importance of developing sustainable production methods. Electrochemical $H_2O_2$ synthesis via the two-electron oxygen reduction reaction ($2e^-$ ORR) has gained attention as a promising alternative to the conventional anthraquinone process. This study introduces a cobalt single-atom catalyst supported on oxygen-functionalized defective $CO_2$-derived porous carbon (Co/O-d-CPC) for $2e^-$ ORR. The electronic structure of the cobalt atoms in the molecular catalysts is modulated due to oxygen dopants in the carbon matrix, enabling them to serve as effective active sites for the $2e^-$ ORR. Density functional theory (DFT) calculations and structural characterizations revealed the critical role of specific oxygen functionalities, specifically, triple-coordinated oxygen groups, in optimizing the cobalt single atoms. The synergistic effect between cobalt and these oxygen groups significantly enhanced the $2e^-$ ORR catalytic performance. The electrocatalyst was evaluated under a wide range of pH conditions and demonstrated an average $H_2O_2$ selectivity of 93% within the voltage range of 0.2–0.45 V vs. RHE in neutral media, with significant performance improvements also observed in acidic and alkaline electrolytes. Notably, in flow cell tests with neutral electrolytes, Co/O-d-CPC achieved an exceptional $H_2O_2$ production rate of 14.4 mol $g^{-1}$ $h^{-1}$ at a constant current of 300 mA $cm^{-2}$.

## 1. Introduction

Sustainable production of chemicals has attracted attention due to safety concerns and greenhouse gas emissions during operation.[1,2] The production of hydrogen peroxide ($H_2O_2$), one of the most environmentally benign oxidizing agents and a key component in wastewater treatment, semiconductor manufacturing, and medical applications, entails significant challenges associated with the anthraquinone process. Approximately 95% of the three million tons of $H_2O_2$ produced annually worldwide is manufactured through the anthraquinone process.[3] However, this process involves complex reprocessing steps and chemical treatments, which give rise to significant environmental issues due to waste generation.[4,5] It also requires excessive energy consumption (8.1 kWh $kg^{-1}$) and relies on high-cost palladium catalysts. These limitations of the anthraquinone process have prompted extensive research into alternative synthesis methods including the direct production of $H_2O_2$ through the reaction of oxygen and hydrogen. However, this approach is hindered by safety concerns due to its partially explosive

* Corresponding author. Extreme Materials Research Center, Korea Institute of Science and Technology, Seoul, 02792, Republic of Korea.
** Corresponding author.
*** Corresponding author.
*E-mail addresses:* jongminkim@kist.re.kr (J.M. Kim), chemekim@hanyang.ac.kr (K. Kim), jaewlee@kaist.ac.kr (J.W. Lee).
Peer review under the responsibility of the editorial board of Materials Reports: Energy.
[1] These authors contributed equally to this work.

https://doi.org/10.1016/j.matre.2026.100431
Received 14 October 2025; Received in revised form 4 January 2026; Accepted 28 January 2026
Available online 15 April 2026
2666-9358/© 2026 The Authors. Publishing services by Elsevier B.V. on behalf of KeAi Communications Co. Ltd. This is an open access article under the CC BY-NC-ND license (http://creativecommons.org/licenses/by-nc-nd/4.0/).

nature and the reliance on expensive noble metal catalysts.[6,7] In contrast, the electrochemical production of $H_2O_2$ via the two-electron oxygen reduction reaction ($2e^-$ ORR) has emerged as a viable alternative, on the basis of its safety. This method provides an environmentally friendly and safe on-site production route, addressing many challenges associated with the anthraquinone process and other alternatives.[8,9] Furthermore, it avoids harmful by-products and organic waste, offering additional environmental benefits while ensuring sustainability.[10,11] Despite their potential, electrochemical synthesis methods are impeded by the scarcity of highly active and cost-effective electrocatalysts. The electrochemical $H_2O_2$ production process has not yet replaced the anthraquinone process in industries that require large-scale production. To address these issues, optimized catalyst structures to enhance the activity and durability of the $2e^-$ ORR process should be developed.[12]

The variation in catalyst performance depending on the pH environment of the electrolyte is also a significant limitation that hinders the practical application of $2e^-$ ORR catalysts. While numerous studies have focused on $2e^-$ ORR in alkaline solution electrolytes in which the catalyst exhibits optimal activity, these conditions promote $H_2O_2$ decomposition at high pH levels and pose challenges related to the long-term stability of anion exchange membranes.[13,14] In contrast, the decomposition of $H_2O_2$ to $H_2O$ is less prevalent in acidic electrolytes, and thus they are commonly used in industrial production. However, the catalyst's activity is significantly lower under acidic conditions.[15,16] Neutral electrolytes meanwhile offer safety and non-corrosiveness, resulting in a more practical and versatile $H_2O_2$ solution for various applications.[17] However, the use of neutral electrolytes is limited by slow ORR kinetics, which lead to high overpotentials and low selectivity.[18] To enhance the efficiency of electrocatalytic $H_2O_2$ synthesis, it is crucial to develop electrocatalysts that can achieve high performance in various electrolyte environments. Such versatility is critical for meeting the specific pH requirements of diverse $H_2O_2$ applications. For example, slightly alkaline conditions are preferred in bleaching, mildly acidic conditions are ideal for disinfection, and strongly acidic environments are often required for wastewater treatment. Maintaining high catalytic performance under varying pH conditions is thus essential for advancing the practicality and efficiency of $H_2O_2$ electrosynthesis.

Carbon-based materials have been extensively explored as electrocatalysts that can address these issues due to their earth abundance, superior electrical conductivity, and electrochemical stability.[19–21] Recent studies have shown that the catalytic performance of carbon materials can be significantly improved by introducing heteroatoms and modifying their structure, especially by adding oxygen functional groups (OFGs).[22,23] Despite the improvements offered by OFGs for $H_2O_2$ production via the $2e^-$ ORR, the potential range for maintaining high selectivity is narrow. This narrow operational window arises from the decomposition of $H_2O_2$ into water caused by increased overpotential and low onset potential.[19,24,25] Furthermore, accurately identifying and optimizing active OFGs remains a substantial challenge that should be addressed to fully realize their catalytic potential. In addition to OFGs, numerous $2e^-$ ORR catalysts have been actively developed in which heteroatoms such as boron serve as active sites within the carbon framework. However, they generally suffer from lower performance in acidic electrolytes, where $H_2O_2$ is most stable.[26]

Along with heteroatom doping, single-atom catalysts (SACs) have garnered considerable attention for their unique electronic structures and high atom-utilization efficiency.[27] Moreover, metal single-atom catalysts offer fast reaction and mass-transport kinetics, enabling high performance even in acidic electrolytes, where an inner-sphere electron transfer pathway is dominant.[28] Among SACs, atomic Co-$N_x$-C sites have been extensively studied and demonstrated high effectiveness. The high performance of Co single atoms has been achieved through atomic-level structural modifications, including the tuning of coordination environments. Approaches to modify the coordination environment of SACs include altering the ligand coordination sphere in structures such as Co-$N_2$ and Co-$N_5$.[29–31] Researchers have also explored incorporating functional groups to modulate the interaction between metal single atom and heteroatom. For example, in Co-POC-O, Co-$N_x$ sites are combined with oxygen-functionalized groups to improve reactivity and selectivity for $H_2O_2$ electrosynthesis.[24] The electronic structure of the metal is altered by the electron cloud of adjacent oxygen atoms, thereby allowing it to achieve enhanced $2e^-$ ORR performance.[32,33] Recent advances, such as the development of Co-$N_2O_2$ coordination structures, highlight the potential of atomic-level modifications to optimize catalytic performance.[34] However, despite ongoing efforts to optimize the coordination environment and the structure of metal catalysts, particularly cobalt SACs, catalysts exhibiting outstanding performance across a wide pH range have not yet been reported.

Herein, we report the development of Co/O-d-CPC, an optimized catalyst for $H_2O_2$ electrosynthesis that integrates an oxygen-functionalized defective $CO_2$-derived carbon support with Co-SACs. In this catalyst, the electronic structure of cobalt is modified by the surrounding oxygen functional groups, and this structural change significantly enhances the $2e^-$ ORR efficiency across neutral, alkaline, and acidic conditions. Notably, Co/O-d-CPC demonstrates approximately 93% $H_2O_2$ selectivity within a potential range of 0.2–0.45 V vs. RHE under neutral conditions. High performance is also observed in both alkaline and acidic environments. Furthermore, the catalyst maintains a steady Faradaic efficiency of 90.5% over 12 h in H-type cell tests conducted under neutral conditions, yielding a $H_2O_2$ production rate of 619.95 mmol $g_{cat}^{-1}$ $h^{-1}$. Additionally, the catalyst has been applied in a flow cell system under three different electrolytes and displayed high $H_2O_2$ selectivity and production rate. Notably, in neutral electrolytes, the Co/O-d-CPC catalyst exhibited an $H_2O_2$ production rate of 14.4 mol $g^{-1}$ $h^{-1}$ at a constant current density of 300 mA $cm^{-2}$. This superior performance is attributed to the synergistic effect between the OFGs on the carbon surface and Co single atoms. The versatility and consistent performance of Co/O-d-CPC underscore its potential for sustainable $H_2O_2$ production. Structural characterization, supported by density functional theory (DFT) calculations, identifies cobalt sites influenced by the triple-coordinated oxygen groups ($O_C$ groups) as predominant active sites. These $O_C$ groups interact with Co-SACs to modify electronic structure of the Co center, modulating the adsorption energy of intermediates and enhancing catalytic performance. These valuable insights into the synergistic roles of modified carbon supports and metal active sites will ultimately benefit the design of efficient electrocatalysts for sustainable $H_2O_2$ production.

## 2. Experimental section

### 2.1. Chemicals

Sodium borohydride ($NaBH_4$, Sigma-Aldrich, >99%), polyethylene oxide (PEO), cobalt(II) phthalocyanine (CoPc), dimethylformamide (DMF, >99.9%), Nafion solution (5 wt%), and cerium(IV) sulfate (Ce$(SO_4)_2$, ≥99.9%) were purchased from Sigma-Aldrich. Potassium hydroxide (KOH, 95%), potassium sulfate ($K_2SO_4$, 99 wt%) and hydrochloric acid (HCl, 37 wt%) were obtained from Samchun. Sulfuric acid ($H_2SO_4$, 98%) was obtained from Daejung. Calcium carbonate nanoparticles ($CaCO_3$, 15–40 nm) was procured from SkySpring Nanomaterials.

### 2.2. Synthesis of Co/O-d-CPC

Co/O-d-CPC was synthesized as shown in Fig. 1a. First, d-CPC (defective $CO_2$-derived porous carbon) was prepared by physically mixing $NaBH_4$ and $CaCO_3$ in a 1:1 mass ratio based on previous works.[35,36] The mixture was heated to 500 °C at a rate of 5 °C $min^{-1}$ under a $CO_2$ flow of 80 mL $min^{-1}$ for 2 h. It was then heated to 700 °C, with the gas flow switched from $CO_2$ to Ar at 600 °C, and held at 700 °C for another 2 h. The resulting product was washed several times with HCl, DI water, and ethanol, and then dried overnight at 80 °C. The

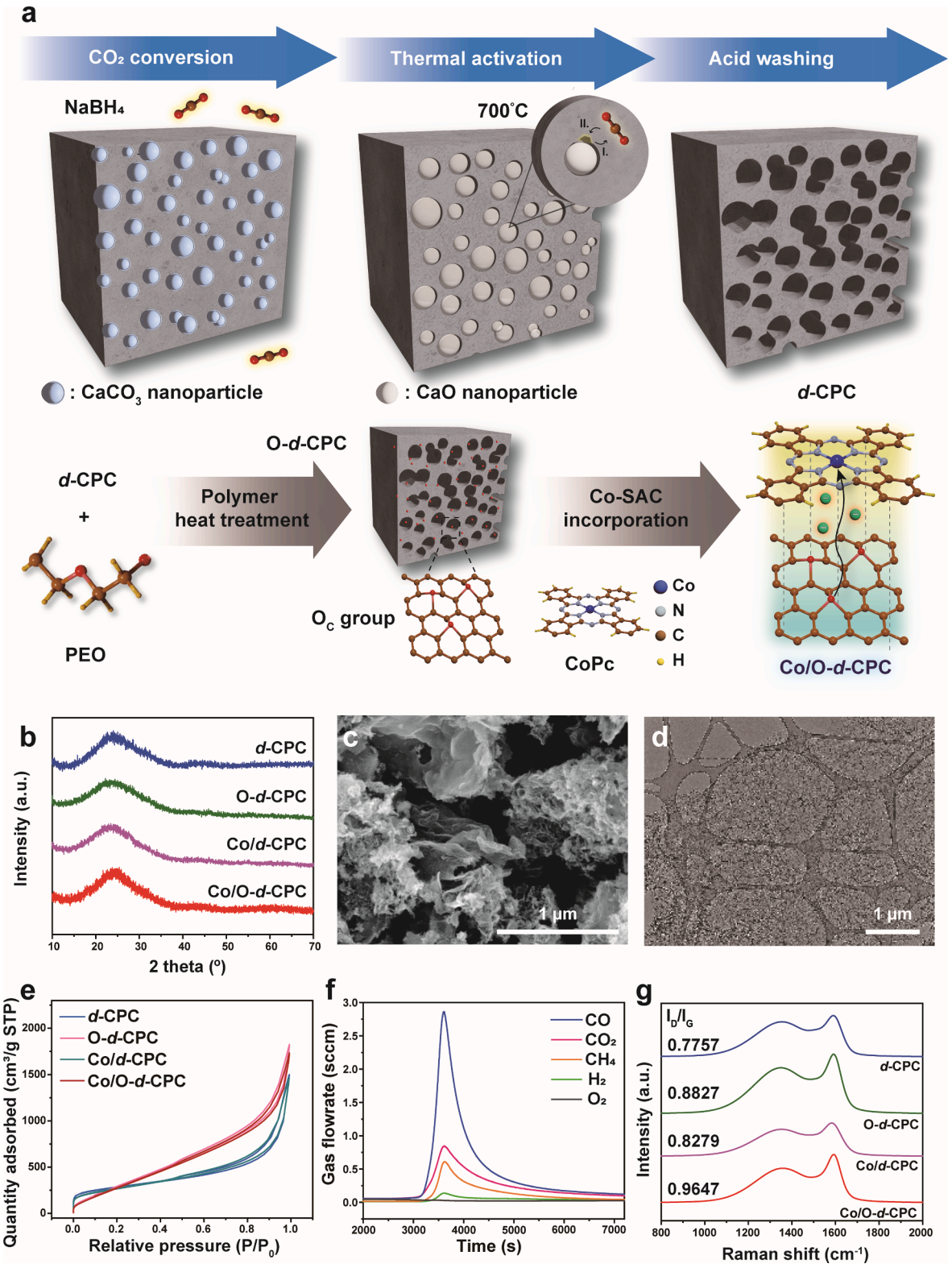


**Fig. 1.** (a) Schematic illustration of the synthesis procedure for d-CPC, O-d-CPC, Co/d-CPC, and Co/O-d-CPC. (b) XRD patterns of d-CPC, O-d-CPC, Co/d-CPC, and Co/O-d-CPC. (c) SEM image of Co/O-d-CPC. (d) Bright field TEM image of Co/O-d-CPC. (e) $N_2$ adsorption/desorption isotherms plot of d-CPC, O-d-CPC, Co/d-CPC, and Co/O-d-CPC. (f) Outlet gas profile during heat treatment of d-CPC with PEO. (g) Raman spectra of d-CPC, O-d-CPC, Co/O-d-CPC, and Co/d-CPC.

obtained material was denoted as d-CPC. To introduce oxygen functional groups, d-CPC was mixed with PEO in a 1:4 mass ratio and heated to 550 °C under an Ar flow for 3 h, forming O-d-CPC. For the final synthesis of Co/O-d-CPC, O-d-CPC was dispersed in DMF and sonicated for 1 h. Then, 0.25 wt% of CoPc (cobalt phthalocyanine) upon the mass of O-d-CPC was added, followed by additional sonication for 1 h. The mixture was stirred for 24 h and then centrifuged at 9000 rpm for 20 min. The obtained materials were washed several times with DMF and ethanol. The product was freeze-dried to obtain Co/O-d-CPC, resulting in weakly anchored CoPc molecules on the O-d-CPC surface.

Co/d-CPC was synthesized following the same procedure as Co/O-d-CPC, using d-CPC instead of O-d-CPC.

### 2.3. Material characterization

The morphology of the catalysts was investigated by scanning electron microscopy (SEM, SU8230) and transmission electron microscopy (TEM, Talos F200X G2). Additionally, an X-ray diffraction (XRD) analysis was carried out using a RIGAKU SmartLab, with a $2\theta$ measurement range from 10° to 80° and a scan rate of 5° $min^{-1}$. Raman analysis was conducted using a RIBA LabRAM HR Evolution Visible NIR spectrometer with a 514 nm laser source, covering a Raman shift range of 300–450 $cm^{-1}$. The specific surface area was measured using the Brunauer-Emmett-Teller (BET) theory with $N_2$ gas adsorption-desorption isotherms at 77 K. The micropore and mesopore volume were determined by the t-plot method and Barrett-Joyner-Halenda (BJH) theory. Extended X-ray absorption fine-structure (EXAFS) analysis at the Co K-edge and soft X-ray absorption near edge structure (XANES) analysis at the O K-edge were conducted at the 1D XRS KIST-PAL beamline at Pohang Accelerator Laboratory, South Korea. The Co K-edge EXAFS data were processed using the IFEFFIT software package to obtain their Fourier-transformed results. High-angle annular dark-field scanning transmission electron microscopy (HAADF-STEM, FEI Talos F200X) was employed to visualize the cobalt single-atom morphology. The outlet gas during the polymer heat treatment was analyzed using a quadrupole mass spectrometer (Pfeiffer Prisma Pro). The presence of single atoms was further confirmed using a Titan double Cs corrected transmission electron microscope (Titan cubed G2 60-300) and time-of-flight secondary ion mass spectrometry (ION-TOF GmbH). Furthermore, the surface elemental composition of the materials was analyzed using a Kratos Axis-Supra instrument for X-ray photoelectron spectroscopy (XPS) measurements. Ultraviolet-visible (UV-Vis) spectra were obtained using a PerkinElmer Lambda1050 spectrophotometer at 319 nm equipped with a quartz cell.

### 2.4. Electrochemical characterization

#### 2.4.1. RRDE analysis

To prepare the catalyst ink for electrochemical measurements, 4 mg of the catalyst was dispersed in 100 μL of a 5 wt% Nafion solution and 1000 μL of ethanol. The mixture was then sonicated for 60 min to ensure a homogeneous dispersion of the catalyst. A 5 μL aliquot of the resulting ink was subsequently deposited onto the glassy carbon disk (area: 0.1256 $cm^2$) of a rotating ring disk electrode (RRDE). The electrochemical setup included the RRDE, consisting of a glassy carbon disk and a platinum ring as the working electrode, an Ag/AgCl reference electrode, and a platinum wire serving as the counter electrode. The catalysts' electrochemical properties were assessed using a Bio-Logic VSP potentiostat within a three-electrode configuration. The experiments were conducted in three different electrolytes: 0.1 M KOH (alkaline), 0.1 M $K_2SO_4$ (neutral), and 0.05 M $H_2SO_4$ (acidic). Before measurements, the electrodes underwent a cleaning process via cyclic voltammetry (CV) at a scan rate of 500 mV $s^{-1}$, sweeping from 0 V to 1.3 V vs. RHE in an argon-saturated solution. Polarization curves were recorded at a rotation speed of 1600 rpm with a scan rate of 10 mV $s^{-1}$ under oxygen-saturated conditions. A constant voltage of 1.2 V vs. RHE was applied to the platinum ring to detect $H_2O_2$ oxidation. Background currents from both the disk and ring electrodes were measured by identical polarization tests in an argon-saturated electrolyte. The true ORR current was calculated by subtracting the background current from the current measured in oxygen-saturated conditions.

The catalyst selectivity towards $H_2O_2$ was determined using Equation (1):

$$\text{Catalyst selectivity of } H_2O_2(\%) = 200 \times \frac{\frac{I_r}{N}}{\frac{I_r}{N} + I_d} \quad (1)$$

where $I_r$ is the Pt ring current, $I_d$ is the glassy carbon disk current, and $N$ is the collection efficiency. $N$ was determined to be 0.445 using a standard redox system with $K_3[Fe(CN)_6]$ solution (Equation (2)):

$$N = \frac{I_r}{|I_d|} \quad (2)$$

The electron transfer number ($n$) for the oxygen reduction reaction was determined using RRDE measurements, delineated in Equation (3).

$$\text{Electrons transferred number } (n) = 4 \times \frac{I_d}{I_d + \frac{I_r}{N}} \quad (3)$$

The kinetic current density ($J_k$) was obtained by applying the Koutecký–Levich method to correct for mass transport effects (Equation (4)):

$$\frac{1}{J_m} = \frac{1}{J_l} + \frac{1}{J_k} \quad (4)$$

The total current density ($J_m$) was experimentally measured, while the diffusion-limited current density ($J_l$) was used to correct for mass transport limitations. Due to the inherent difficulty in determining the maximum steady-state current over the full potential range for most carbon-based catalysts, the limiting current was calculated using the Levich equation (Equation (5)), which is based on the electron transfer number ($n$) obtained from the RRDE data:

$$J_l = 0.62nFAD_0^{2/3}\omega^{1/2}\nu^{-1/6}C_0 \quad (5)$$

The constants and parameters used in these calculations include the Faraday constant ($F$, 96,485 C $mol^{-1}$), the geometric area of the disk electrode ($A$, 0.1256 $cm^2$), the diffusion coefficient of $O_2$ in the electrolyte at 298 K ($D_0$, $1.85\times10^{-5}$ $cm^2$ $s^{-1}$), the electrode rotation speed (ω, 167.55 rad $s^{-1}$), the kinematic viscosity of $O_2$ ($\nu$, $0.89\times10^{-2}$ $cm^2$ $s^{-1}$), and the concentration of $O_2$ ($C_0$, $1.21\times10^{-6}$ mol $cm^{-3}$).

#### 2.4.2. H-cell test

The oxygen reduction reaction (ORR) was evaluated using a H-cell to measure $H_2O_2$ production, Faradaic efficiency (FE), and catalyst stability under various experimental conditions. A two-chamber H-cell system separated by a Nafion 117 ion exchange membrane was used. Each chamber contained 40 mL of 0.1 M $K_2SO_4$ electrolyte solution. The working electrode, carbon paper (1 cm×1 cm) loaded with 0.1 mg of Co/O-d-CPC, and the Ag/AgCl reference electrode were positioned in one chamber, while a graphite rod served as the counter electrode in the opposite chamber.

The cathode chamber was purged with argon gas before cyclic voltammetry (CV) was used to activate the working electrode by scanning the potential range from 0 V to 1.0 V vs. RHE at a scan rate of 50 mV $s^{-1}$. Following activation, the solution was saturated with oxygen for 1 h. Chronoamperometry (CA) measurements were then performed at a fixed potential of 0.3 V vs. RHE, with the cathode chamber stirred at 400 rpm. The amount of $H_2O_2$ produced during the ORR was determined through titration with cerium sulfate ($Ce(SO_4)_2$). In this process, the $H_2O_2$ reacts with $Ce^{4+}$ ions, reducing them to $Ce^{3+}$, as described in Equation (6).

$$2Ce^{4+} + H_2O_2 \rightarrow 2Ce^{3+} + 2H^+ + O_2 \quad (6)$$

This redox reaction is used for $H_2O_2$ detection, as the reduction of $Ce^{4+}$ to $Ce^{3+}$ can be monitored via UV-Vis spectroscopy. Every hour, 50 μL aliquots from the electrolyte were extracted and mixed with 4 mL of 0.5 mM $Ce(SO_4)_2$ solution prepared in 0.5 M $H_2SO_4$. The $H_2O_2$ concentration was quantified by measuring the decrease in $Ce^{4+}$ concentration using UV-Vis spectroscopy. This analysis was performed over a wavelength range of 300–800 nm. A calibration curve was established by analyzing $Ce(SO_4)_2$ solutions with known concentrations (0–0.5 mM), with absorbance measured at 319 nm, in accordance with Equation (7).

$$Abs = \varepsilon \times l \times \left[Ce^{4+}\right] \quad (7)$$

Here, Abs refers to the absorbance at 319 nm, $[Ce^{4+}]$ represents the concentration of $Ce^{4+}$ (mM), $\varepsilon$ denotes the molar absorptivity of $Ce^{4+}$ ($mM^{-1}$ $cm^{-1}$), and $l$ is the path length of the cuvette (cm).[3]

The FE was calculated based on the $H_2O_2$ concentration in the H-cell, using the formula in Equation (8).

$$\text{FE}\ (\%) = 100 \times \frac{2 \times \text{Total amount of generated } H_2O_2 \times \text{Faraday constant}}{\text{Total amount of charge} \left( \int_0^t J\, dt \right)} \quad (8)$$

where $\left( \int_0^t J\, \mathrm{d}t \right)$ is the total charge passed during the reaction.

### 2.4.3. Flow cell test

A three-electrode flow cell with separate compartments for the oxygen evolution reaction (OER) and ORR was used to evaluate $H_2O_2$ production. The working electrode was prepared by spray-coating a catalyst ink (3 mg catalyst, 50 μL 5% Nafion, 2.25 mL ethanol) onto a 2.3×2.3 $cm^2$ carbon paper gas diffusion layer (0.3 mg $cm^{-2}$ loading). The electrode was dried at 80 °C, and the active area was 2 $cm^2$.

During testing, $O_2$ was supplied to the cathode at 20 mL $min^{-1}$, and the electrolyte was circulated at 40 mL $min^{-1}$ in both compartments. Constant current densities ranging from 10 mA $cm^{-2}$ to 400 mA $cm^{-2}$ were applied using 1 M KOH (pH 14), 1 M $Na_2SO_4$ (pH 7), and 0.5 M $H_2SO_4$ (pH 0.3) electrolytes with appropriate reference (Hg/HgO or calomel) and counter electrodes (NiFeMo foil or Ir foil).

Catholyte samples were periodically collected and titrated with $Ce^{4+}$ to quantify $H_2O_2$. The titration and UV-Vis analysis followed the same procedure as the H-cell test, with the $H_2O_2$ concentration determined using Equation (9):

$$H_2O_2 \text{ concentration} = \frac{\left[Ce^{4+}\right]_{\text{before}} - \left[Ce^{4+}\right]_{\text{after}}}{2 \times V_{\text{titration}}} \times 4.5 \quad (9)$$

For quantification after 1 h of electrolysis, an aliquot of the working electrode electrolyte (5 μL for 20–400 mA and 1 μL for 600 mA) was sampled and added to 4.5 mL of $Ce^{4+}$ stock solution in 0.5 M $H_2SO_4$, $V_{\text{titration}}$ (mL) represents the volume of electrolyte sampled from the 40 mL KOH solution for titration. The absorbances of the $Ce^{4+}$ stock solution at 319 nm were measured both before and after injecting the $H_2O_2$-containing aliquot, denoted as $[Ce^{4+}]_{\text{before}}$ and $[Ce^{4+}]_{\text{after}}$, respectively. The Faradaic efficiency (FE) was calculated using the same equation as employed in the H-cell test. The $H_2O_2$ yield (mol) and production rate (mol $g^{-1}$ $h^{-1}$) were calculated as follows:

$$H_2O_2 \text{ yield} = H_2O_2 \text{ concentration} \times 40 \quad (10)$$

$$H_2O_2 \text{ production rate} = \frac{H_2O_2 \text{ production yield}}{\text{catalyst loading}} \quad (11)$$

To assess the stability of Co/O-d-CPC under neutral conditions, a 500 mL solution of 1 M $Na_2SO_4$ was continuously circulated, and constant current testing at 200 mA was conducted for 30 h with 100% IR compensation applied every hour. Faradaic efficiency was measured during the test using the titration method described earlier. After each chronopotentiometry test, an aliquot of the electrolyte was extracted from the 1 M $Na_2SO_4$ solution and added to a stock solution containing a known concentration of $Ce(SO_4)_2$ in 0.5 M $H_2SO_4$ for UV-Vis analysis.

## 2.5. Computational details

Spin-polarized density functional theory (DFT) calculations were performed using the Vienna Ab-initio Simulation Package (VASP) software with projector-augmented wave (PAW) method to describe core-valence electron interactions.[37,38] The Perdew-Burke-Ernzerhof (PBE) functional with the generalized gradient approximation (GGA) was employed.[39] The plane-wave kinetic cutoff energy was set to 450 eV to the exchange-correlation energies. Gamma-centered k-point grids of 15×15×1 and 1×1×1 were used for unit cell and supercell calculations, respectively. All atoms were fully relaxed until the forces and electronic energies converged to less than 0.01 eV $Å^{-1}$ and $10^{-5}$ eV, respectively. DFT-D4 of Grimme was used for van der Waals (vdW) dispersion corrections. The VASPsol package was used to correct for the implicit solvation effect of water (dielectric constant of 78.5) on the surfaces and reaction intermediates.[40,41] To build various computational models, we used a 10×10 supercell of graphene monolayer unit cells with a 25 Å vacuum layer along the z-axis. The detailed procedures for the computational models are described in the Supplementary material.

$O_2$ reduction to $H_2O_2$ ($2e^-$ ORR) can be expressed as two elementary reactions[42]:

$$O_2(g) + 2H^+ + 2e^- + * \longrightarrow OOH^* + H^+ + e^- \quad (12\text{-}1,\ R1)$$

$$OOH^* + H^+ + e^- \longrightarrow H_2O_2(g) + * \quad (12\text{-}2,\ R2)$$

Based on the computational hydrogen electrode (CHE) model, the change of Gibbs free energy at each elementary step of the $2e^-$ ORR was calculated by the following equation:

$$\Delta G = \Delta E + \Delta ZPE - T\Delta S + \Delta G_U + \Delta G_{pH} \quad (13)$$

where $\Delta E$, $\Delta ZPE$, $T\Delta S$, $\Delta G_U$, and $\Delta G_{pH}$ indicate the DFT-calculated reaction energy, zero-point energy, the entropic effects on 298.15 K, the effect of applied bias (-neU), and the correction term for the $H^+$ ion contribution at various pH conditions. $\Delta G_{pH}$ can be expressed as the following equation:

$$\Delta G_{pH} = -k_B T \ln[H^+] = -k_B T \ln 10 \times \text{pH} \quad (14)$$

The pH value is set to 7.0 (neutral condition) in our DFT calculations. $k_B$ and $[H^+]$ denote the Boltzmann constant and the concentration of $H^+$ ions. The Bader charge and crystal orbital Hamilton population (COHP) calculations were performed based on Henkelman group's code and the LOBSTER package, respectively.[43–47]

# 3. Results and discussion

## 3.1. Structural and physicochemical properties

The crystalline properties of the materials were characterized by X-ray diffraction (XRD) analysis. The XRD patterns exhibited broad peaks at around 24° and 43°, which correspond to the (002) and (100) diffraction planes typically associated with carbonaceous materials exhibiting a partially layered structure. These broad peaks suggest an amorphous structure, as shown in Fig. 1b.[48,49,50]

SEM investigation of Co/O-d-CPC revealed minimal structural changes compared to the initial d-CPC (Fig. 1c, Fig. S1a). The structures of O-d-CPC and Co/d-CPC (Fig. S1b-c) demonstrate a consistent hierarchical porous structure without significant variations across all the samples. This porous structure is formed by the nanostructured template, $CaCO_3$, which is confirmed by TEM images (Fig. 1d, Fig. S2a-c). The stability of the porous structure is demonstrated by its preservation after high-temperature treatment and polymer pyrolysis.

The pore distribution of the four carbon materials was analyzed using Brunauer–Emmett–Teller (BET) method, with results presented as $N_2$-sorption isotherms (Fig. 1e), NLDFT pore distributions (Fig. S3), and BET surface areas with pore volumes (Table S1). The isotherms exhibit adsorption at low pressures ($P/P° < 0.001$), which is indicative of micropore adsorption. At medium-to-high relative pressures (0.5–1.0 $P/P°$), a noticeable hysteresis loop is observed, suggesting a porous structure with interconnected or irregularly shaped mesopores. This

pore structure is activated during the d-CPC synthesis process (Fig. 1a), including $CO_2$ reduction to carbon material.[9,51] Furthermore, the thermal decomposition of $CaCO_3$ and subsequent $CO_2$ activation contribute to the high porosity of the $CaCO_3$-templated porous carbon.[36] At 700 °C, $CaCO_3$ decomposes into $CO_2$ and CaO (Equation (15)), and the released $CO_2$ reacts with surrounding carbon to produce CO (Equation (16)). This $CO_2$ activation process accounts for the unique hierarchical porosity observed in d-CPC. Consequently, d-CPC exhibits a highly porous structure with a total pore volume of 2.323 $cm^3\ g^{-1}$ and a surface area of 1001.65 $m^2\ g^{-1}$.

$$CaCO_3 \rightarrow CO_2 + CaO \quad (15)$$

$$CO_2 + C \rightarrow 2CO \text{ (reverse Boudouard reaction)} \quad (16)$$

The BET surface area of Co/d-CPC slightly decreases to 925.78 $m^2\ g^{-1}$ due to anchored CoPc, although this difference is not significant. Also, O-d-CPC and Co/O-d-CPC show further decrease in surface area to 890.39 $m^2\ g^{-1}$ and 844.70 $m^2\ g^{-1}$, respectively. The micropore volume for d-CPC and Co/d-CPC was measured as 0.1521 $cm^3\ g^{-1}$ and 0.1423 $cm^3\ g^{-1}$, respectively, while O-d-CPC and Co/O-d-CPC show reduced volumes of 0.05468 $cm^3\ g^{-1}$ and 0.03829 $cm^3\ g^{-1}$. The reduction in micropore volume appears to be the primary cause of the decreased surface area. Conversely, both O-d-CPC and Co/O-d-CPC have increased mesopore volumes compared to d-CPC and Co/d-CPC (Fig. S4). Mesopores provide advantages for the $2e^-$ ORR compared to micropores by facilitating mass transfer of reactants and products. This larger pore size prevents $H_2O_2$ from being trapped, thus minimizing its further undesired reduction to $H_2O$.[51–53] To identify the cause of the increase in the mesopore volume, the material was synthesized using the same method as employed for O-d-CPC with oxygen-free polymer polyethylene (PE) instead of PEO. The PE-treated sample also exhibited enlarged mesopore volumes and reduced micropore volumes relative to d-CPC, similar to O-d-CPC (Table S1). These findings confirm that the mesopore enhancement can be primarily attributed to the polymer-assisted thermal treatment.

To investigate the mechanism underlying these observations, mass spectrometry (MS) was conducted to analyze the outlet gases during the polymer heat treatment process at 500 °C under Ar gas. The MS analysis revealed that CO and $CO_2$ gases were released during the heat treatment of both PE and PEO (Figs. 1f and S5, Table S2), while almost no gas was released when d-CPC was heat-treated without any polymer (Fig. S6). The polymer-derived CO and $CO_2$ activate the carbon matrix and create mesoporous structures. Interestingly, despite differences in gas release quantities between PE and PEO, both treatments resulted in similar mesopore volumes. This is due to the low thermal decomposition temperature of the polymer. At low temperatures, most gases are released; however, the temperature is insufficient to drive reactions that increase the volume. Consequently, at higher temperatures, where the carbon matrix and gas undergo the mesopore-expanding reactions described in Equations (15) and (16), only a small fraction of the polymer decomposes and participates.[35] Polymer-free d-CPC, which did not release these gases (Fig. S6) and lacked interactions between the gas and carbon, exhibited only limited meso-porosity, further demonstrating the importance of polymer-derived gases in this process.

Raman spectroscopy was performed to analyze the defect distribution in the four materials. As illustrated in Fig. 1g, all samples displayed characteristic peaks for the D-band at 1350 $cm^{-1}$ and the G-band at 1590 $cm^{-1}$, which are predominantly observed in carbon materials. The D-band is associated with disorder in $sp^2$–hybridized carbon whereas the G-band is associated with carbon-carbon bonds within the graphite plane. The lowest $I_D/I_G$ ratio was observed for d-CPC at 0.7757, whereas O-d-CPC and Co/d-CPC had higher ratios of 0.8827 and 0.8279, respectively. These increases are attributed to the introduction of oxygen functionalities via PEO thermal treatment as well as to additional defects induced by the anchoring of CoPc onto the carbon. Strong adsorption of CoPc on the carbon framework, particularly at the edge of layer, leads to an increase in the $I_D/I_G$ ratio. Notably, Co/O-d-CPC demonstrated the highest $I_D/I_G$ at 0.9647, reflecting the enhanced defect density resulting from the combined effects of PEO polymer treatment and CoPc incorporation.

### 3.2. Catalyst composition and Co-SACs

The coordination environment and chemical state of Co atoms were analyzed using X-ray absorption near-edge structure (XANES, refer to Fig. S7) and extended X-ray absorption fine structure (EXAFS).The first derivative XANES spectra in Fig. 2a reveal that Co/O-d-CPC exhibits a higher positive peak position compared to CoO ($Co^{2+}$) and $Co_3O_4$ (mixed $Co^{2+}/Co^{3+}$, average oxidation state of +2.67), and indicate an estimated oxidation state of +2.7 or higher for cobalt. Moreover, Co/O-d-CPC shows a higher absorption edge energy than Co/d-CPC, further supporting a more positively charged cobalt center. The Fourier-transformed (FT) $k^2$-weighted EXAFS spectra in Fig. 2b demonstrate a main peak at approximately 1.5 Å, corresponding to the Co–N first coordination shell, with no observable Co–Co coordination peak near 2.16 Å for both Co/O-d-CPC and Co/d-CPC. Thus, Co/O-d-CPC and Co/d-CPC exhibit the same peak pattern as CoPc, which features a Co-N structure. This confirms that Co exists in a single-atom structure in both Co/O-d-CPC and Co/d-CPC. The fitting curves of the EXAFS results are shown in the Supplementary material (Figs. S8 and S9). The coordination number analysis revealed changes upon the introduction of oxygen functional groups (Table S3). Co/d-CPC exhibits a Co-N coordination number of 4.2 ± 0.9, indicating a more complete Co-$N_4$ structure compared to Co/O-d-CPC, where Co-N coordination decreases to 3.6 ± 0.4 due to competitive interactions between N and O around Co. Furthermore, Co–C coordination for Co/O-d-CPC (9.8 ± 2.6) is significantly higher than for Co/d-CPC (2.3 ± 0.6), suggesting enhanced stability of Co-$N_4$ moieties with the carbon matrix upon oxygen doping. As shown in the Wavelet transform (WT)–EXAFS plot (Fig. S10), the materials featuring Co–N coordination (CoPc, Co/d-CPC, and Co/O-d-CPC) exhibit strong intensity centered around ~4 $Å^{-1}$. In contrast, other non-single atom reference samples (CoO and $Co_3O_4$) exhibit significant intensity at 5.4 $Å^{-1}$, indicating Co–O coordination and structural differences with others. Additionally, Co/O-d-CPC, in contrast to Co/d-CPC without O-doping, clearly exhibited Co–O shells in the EXAFS analysis due to the oxygen functionalization.

Dark-field STEM and EDS mapping analyses of Co/O-d-CPC demonstrate a uniform distribution of oxygen. The mapping data further illustrates a homogeneous dispersion of cobalt and nitrogen, indicating well-distributed CoPc (Fig. 2c, refer to Fig. S11 for Co/d-CPC). HAADF-STEM imaging also reveals distinct bright spots corresponding to isolated cobalt single atoms uniformly distributed within the carbon matrix, as highlighted by yellow circles in Fig. 2d (refer to Fig. S12 for Co/d-CPC).

The surface composition was determined using XPS analysis. The full-survey XPS spectra (Fig. S13) showed that O-d-CPC subjected to PEO treatment exhibited a lower oxygen content than d-CPC (Table S4). This is because the additional heat treatment required for oxygen doping of d-CPC induced the loss of oxygen from the pre-existing carbon matrix. This heteroatom release also occurred for boron during the heat treatment with PEO, leaving only a trace amount detectable by XPS in O-d-CPC. However, while the heat-treatment-assisted oxygen doping causes the loss of heteroatoms, it simultaneously introduces oxygen functional groups with new configurations not present in the pristine material. In particular, oxygen functional groups associated with bonds originating from defect structures formed during the heat treatment and additional doping are newly introduced. In both Co/d-CPC and Co/O-d-CPC, nitrogen species originating from CoPc anchored on the carbon matrix were observed. A higher nitrogen content was found in Co/d-CPC compared to Co/O-d-CPC, which was attributed to the relatively larger number of heteroatoms and the more stable carbon matrix in d-CPC, which facilitated the more extensive anchoring of CoPc. This

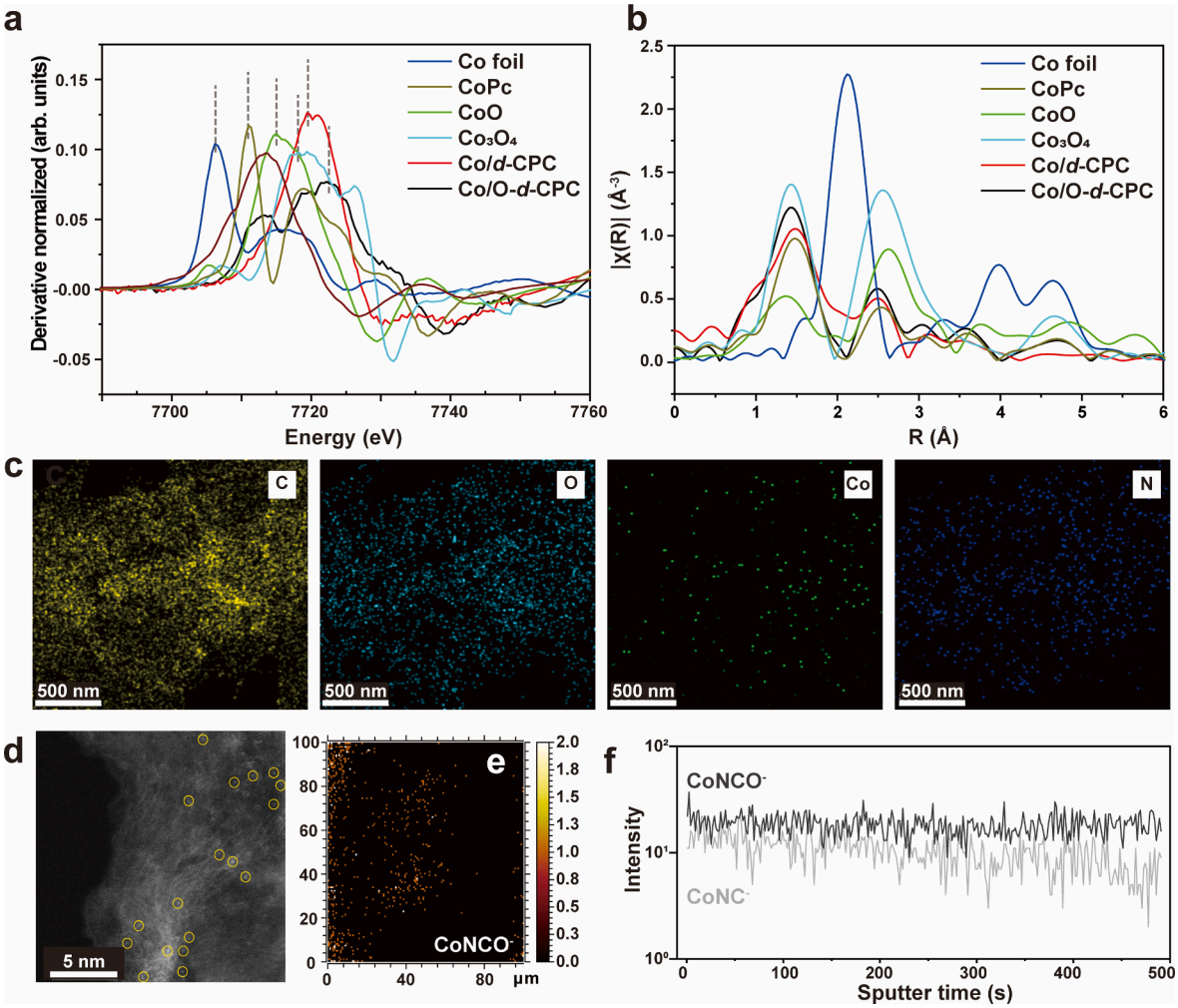


**Fig. 2.** (a) First derivative XANES spectra at the Co K-edge for Co foil (black), CoPc (sky blue), CoO (green), $Co_3O_4$ (yellow), Co/d-CPC (blue), and Co/O-d-CPC (red). (b) Fourier-transformed (FT) EXAFS spectra in R-space for the corresponding samples. (c) Dark-field STEM image of Co/O-d-CPC with corresponding C, O, Co, and N elemental mapping images. (d) HAADF-STEM image of Co/O-d-CPC, showing isolated Co single atoms (bright spots marked by yellow circles) dispersed in the carbon matrix. (e) TOF-SIMS (negative ion mode) image showing $CoNCO^-$ ions of Co/O-d-CPC. (f) TOF-SIMS analysis (negative ion mode) showing intensity vs. sputter time for Co/O-d-CPC.

difference in the stabilization of CoPc on each material led to variations in the electronic structure of Co. In the high-resolution Co 2p spectra shown in Fig. S14, the Co 2p peak of Co/O-d-CPC is shifted to a slightly higher binding energy than that of Co/d-CPC. This indicates that the oxidation state of Co in Co/O-d-CPC is relatively higher, which is consistent with XANES results. However, TOF-SIMS analysis revealed that CoPc directly anchored to oxygen functional groups was more abundant in Co/O-d-CPC. To investigate this, a TOF-SIMS analysis (negative ion mode) was conducted to identify the bonding environment of oxygen in the carbon materials. The increased $CoNCO^-$ ion ratio suggests enhanced oxygen coordination around CoPc as shown in Fig. 2e (Figs. S15–S16). Specifically, the $CoNCO^-/CoNC^-$ ratio indicates the proportion of CoPc anchored on the carbon matrix that is directly associated with oxygen functional groups. The elevated $CoNCO^-/CoNC^-$ ratio observed for Co/O-d-CPC suggests a higher abundance of oxygen functional groups with strong affinity toward CoPc compared to d-CPC (Figs. 2f and S17, Table S5). A TOF-SIMS analysis of $OC^{3-}$ ions was also performed, where the higher signal ratio observed in the Co/O-d-CPC sample corresponds to a newly doped configuration generated through heat treatment with PEO. (Fig. S18). This result indicates that Co/O-d-CPC contains a higher proportion of oxygen species coordinated with three carbon atoms ($O_C$ groups) than in Co/d-CPC.

These findings suggest that, while the total surface oxygen content remains similar across samples, the PEO treatment significantly modifies the oxygen bonding environment. The oxygen functional groups introduced by the PEO treatment lead to strong interactions with CoPc.

### 3.3. DFT simulations

We constructed computational models for DFT simulations, starting with a defective graphene layer (Fig. S19a) and incorporating three types of O-functional groups. Based on the type of functional group, the models were designated as ether (Fig. S19b), epoxy (Fig. S19c), and oxygen-substituted carbon ($O_C$) (Fig. S19d).

To evaluate the effects of the O-functional group concentration, we constructed the most thermodynamically stable computational models containing one to four defects for each type of O-related defect (Figs. S20 and S21). We considered possible adsorption sites of the CoPc molecule in these models (Figs. S22 and S23) and identified the most stable configurations with an adsorbed CoPc molecule (Figs. S24-S26).

To elucidate the role of oxygen functional groups in Co/d-CPC (Fig. S24a) in enhancing the catalytic activity of $2e^-$ ORR, we conducted spin-polarized DFT calculations. As well-known oxygen functional groups in graphene, we considered ether (Fig. S24b–e) and epoxy (Fig. S25) because they have been extensively studied as active sites for the $2e^-$ ORR. In addition, we also considered the oxygen substitution

model ($O_C$), where a carbon atom in graphene is substituted with an oxygen atom(s) (Fig. S19d) because triple-coordinated oxygen has been experimentally observed and exhibits remarkable stability in graphene oxide under high-energy electron beams.[54] Given that the oxygen functional groups were introduced via the high-temperature treatment of defect-rich 3D carbon, the formation of $O_C$ also results in a possible oxygen defect. Thus, we investigated the catalytic activity of Co/d-CPC with different oxygen functional groups for the $2e^-$ ORR.

The $2e^-$ ORR reaction generally consists of two steps: the formation of *OOH from $O_2$ (R1) and the production of $H_2O_2$ from *OOH (R2). The difference of in the Gibbs free energies for both R1 ($\Delta G_{R1}$) and R2 ($\Delta G_{R2}$) are derived from the *OOH adsorption free energy ($E_{*OOH}$), and it is known that the experimentally measured catalytic activity of the $2e^-$ ORR and DFT-calculated $E_{*OOH}$ shows a volcano-like relationship.[4,55] Therefore, the electrochemical activity of the $2e^-$ ORR could be predicted by $E_{*OOH}$. In this context, we also calculated $E_{*OOH}$ in our simulation models (Figs. S27–30, Table S6). In the volcano-like relationship (Fig. 3a), the $H_2O_2$ formation step (R2) becomes the potential-determining step (PDS) of the $2e^-$ ORR pathway when $E_{*OOH}$ is below 4.23 eV, while the *OOH formation step (R1) acts as PDS when $E_{*OOH}$ is higher than 4.23 eV (Fig. 3a).

As shown in Fig. 3a, the introduction of ether and epoxy groups to Co/d-CPC could not effectively tune $E_{*OOH}$ toward the optimal point of the volcano plot. In contrast, as the number of oxygen-substituted carbon atoms ($O_C$) in d-CPC increased from one to four, $E_{*OOH}$ was continuously weakened and shifted closer to the optimal catalytic activity region. This suggests that the formation of $O_C$ in Co/d-CPC (Co/$O_C$) effectively contributes to the high catalytic activity of the $2e^-$ ORR. To decouple the individual contributions of CoPc and $O_C$ to the enhanced catalytic activity of the Co/$O_C$, we also calculated $E_{*OOH}$ on (1–4) $O_C$ models in the absence of CoPc (Fig. S30). The results showed an excessively weak $E_{*OOH}$, indicating that the improved catalytic activity stems from the synergistic effect of the formation of $O_C$ and the introduction of the CoPc molecule on the d-CPC.

The electronic structure analysis revealed that the p-band center of oxygen in the O-groups downshifts in the order of epoxy, ether, and $O_C$ (Fig. S31a). Furthermore, ether and epoxy withdrew electrons from the CoPc molecule, whereas Oc donated electrons to the CoPc molecule (Fig. 3b and Fig. S31b). For this reason, the interaction between the O-functionalized graphene and CoPc molecule, which can be represented by the adsorption energy of the CoPc molecule ($E_{ad}$(CoPc)) on d-CPC was also weakened and strengthened on ether or epoxy functionalized Co/d-CPC and $O_C$, respectively (Fig. S31c). The introduction of $O_C$ into d-CPC thus enhances the anchoring strength of the CoPc molecule, thereby contributing to improved catalytic stability.

To understand the mechanism underlying the effect of interaction between d-CPC and CoPc on the catalytic activity of $2e^-$ ORR, we analyzed the magnetic moment of the Co atom in CoPc, which serves as the active site for the $2e^-$ ORR. Previous studies on Fe-$N_4$ catalysts have demonstrated that the magnetic moment of metal centers directly reflects their spin states and significantly influences the adsorption energies of OER/ORR intermediates, thereby affecting the catalytic activity.[56,57] Our results show that the Co atom in Co/d-CPC has a magnetic moment of approximately 0.863 $\mu_B$ (Fig. 3c, gray dotted line),

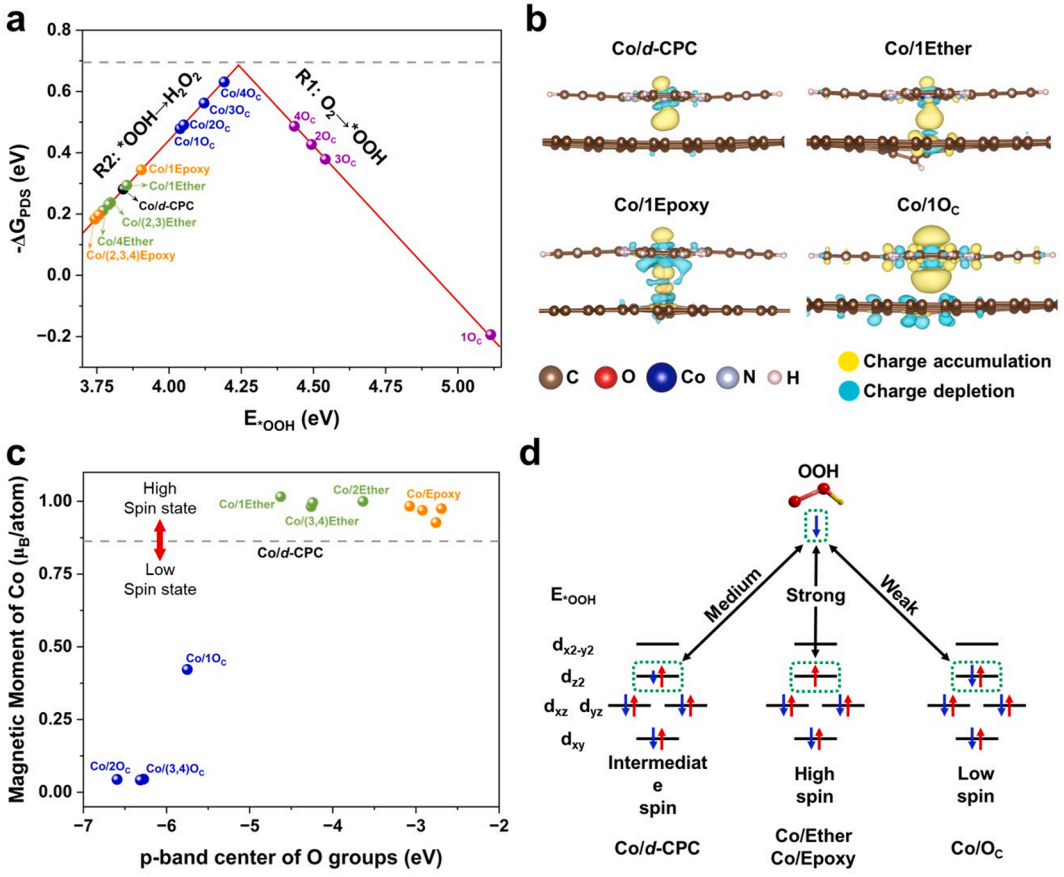


**Fig. 3.** (a) DFT-calculated volcano plot of $2e^-$ ORR. $\Delta G_{PDS}$ and $E_{*OOH}$ indicate the free energy barrier at potential-determining step (PDS) and OOH adsorption free energy, respectively. The equilibrium potential for $2e^-$ ORR (0.695 V vs. RHE) is shown as a gray dashed line. (b) Charge density difference plot of Co/d-CPC, Co/1Ether, Co/1Epoxy, and Co/1$O_C$. Yellow and blue isosurface indicate charge accumulation and depletion, respectively. All charge density difference plots are represented with the same isosurface level. (c) Relation between the p-band center of O functional groups and the magnetic moment of Co atom (Mag(Co), in $\mu_B$). (d) The schematic illustration of spin configurations of Co/d-CPC, Co/Ether, Co/Epoxy, and Co/$O_C$ and $E_{*OOH}$.

suggesting the presence of an unpaired electron. However, electron donation from $O_C$ to the Co atom reduces the magnetic moment of Co to nearly zero (Fig. 3c). In contrast, ether and epoxy groups withdraw electrons from the Co atom. Thus, they enhance the unpaired electron character of Co (Fig. 3c).

Our projected density of states (pDOS) analysis also shows that Co/d-CPC, Co/1Ether, and Co/1Epoxy possess an unpaired electron in the Co $d_{z2}$ orbital (Fig. S32). In the case of $O_C$, as the number of $O_C$ groups increased from one to two, more charge was transferred from the $O_C$ groups to the Co atom, effectively coupling with the unpaired electron in the $d_{z2}$ orbital of the Co atom (Fig. S32). Based on the above analysis, the spin configurations of the Co atom in Co/d-CPC, Co/Ether, Co/Epoxy, and Co/$O_C$ are illustrated in Fig. 3d. We observed that the low-spin state of Co in Co/$O_C$ corresponds to a weaker $E_{*OOH}$ compared to Co/d-CPC (Fig. 3a). Conversely, Co/Ether and Co/Epoxy, which possess a strong unpaired electron character, generally exhibit a stronger $E_{*OOH}$ than Co/d-CPC. This suggests that an unpaired electron of Co can strongly bind with the unpaired electron of OOH (Fig. S33) via spin coupling.[56,57]

To deeply understand the bonding nature between Co and *O in *OOH, we performed crystal orbital Hamilton population (COHP) analyses. A positive (negative) –COHP indicates the bonding (anti-bonding) states of the Co–*O interaction. Our projected COHP (pCOHP) analysis shows that in Co/d-CPC, Co/1Ether, and Co/1Epoxy, up- and down-spin channels contribute equally to the Co–*O interaction (Fig. S34a–c). Even in Co/1$O_C$, which possesses a slightly unpaired electron (Fig. 3c), the up- and down-spin channels contribute almost equally to the Co–*O pair in *OOH–Co/1$O_C$ (Fig. S34d). In contrast, in Co/2$O_C$, which has a low magnetic moment of 0.044 $\mu_B$, the up- and down-spin channels present different contributions, and the down-spin channel shows a notably increased antibonding state compared with the up-spin channel. These findings confirm a weaker Co–*O interaction and insufficient spin coupling (Fig. S34e).

Similar to previous reports that a downshift in the p-band center leads to stronger adsorption of adsorbate, we observed that as the p-band center of oxygen-containing groups in d-CPC downshifts from epoxy to $O_C$ (Fig. S31a), the amount of electron transfer to Co in CoPc molecule increases accordingly (Fig. S31b).[58] $O_C$ with the lowest p-band center donates electrons to the CoPc molecule, while ether and epoxy with higher p-band centers withdraw electrons (Fig. S31b). This enhanced charge transfer from $O_C$ to the Co atom consequently strengthens the adsorption energy of CoPc ($E_{ad}$(CoPc)) (Fig. S31c). Subsequently, this charge transfer process modulates the magnetic moment of Co (Fig. 3c), thereby influencing $E_{*OOH}$ (Fig. 3a). The detailed values of $E_{ad}$(CoPc), the magnetic moment of Co (Mag(Co)), the Bader charge of Co (Bader(Co)), and the p-band center of oxygen are provided in Table S6.

In summary, our DFT calculations demonstrate that introducing $O_C$ into d-CPC enhances the interaction with CoPc, transitions the Co atom in CoPc to a low-spin state, and thereby weakens $E_{*OOH}$. This modification effectively positions the catalyst within the optimal region for high 2e$^-$ ORR activity, providing a strategy for the rational design of efficient peroxide-generating catalysts.

### 3.4. Electrochemical analysis

#### 3.4.1. Electrocatalytic ORR performance evaluation

To evaluate the electrochemical performance for $H_2O_2$ synthesis, rotating ring-disk electrode (RRDE) measurements were performed in three $O_2$-saturated electrolytes: 0.1 M KOH, 0.1 M $K_2SO_4$, and 0.05 M $H_2SO_4$, at a rotation speed of 1600 rpm. The collection efficiency of the RRDE electrode was experimentally evaluated and determined to be 0.445 (Fig. S35).

Under alkaline conditions, as illustrated in Fig. 4a, O-d-CPC, Co/d-CPC, and Co/O-d-CPC exhibited substantial increases in disk and ring current densities across the potential range relative to d-CPC. This enhancement was accompanied by a notable increase in $H_2O_2$ selectivity (Fig. 4d). In the case of O-d-CPC, the introduction of oxygen functional groups to the carbon structure resulted in increased mesopore volume. These mesopores optimize oxygen transport and facilitate the release of $H_2O_2$ while preventing its decomposition into water, thus promoting $H_2O_2$ production. For Co/d-CPC, the dispersion of CoPc significantly improved both 2e$^-$ ORR selectivity and catalytic activity. Notably, Co/O-d-CPC exhibited the most pronounced 2e$^-$ ORR performance. This is attributed to the synergistic effects between OFGs introduced through the polymer heat treatment and anchored CoPc molecules. This synergy resulted in a significant increase in both current density and $H_2O_2$ selectivity, with the latter reaching approximately 90% within the potential range of 0.5–0.8 V vs. RHE.

As shown in Fig. 4b and e, under neutral conditions, Co/O-d-CPC exhibited significantly sustained high $H_2O_2$ selectivity across the entire potential range compared to d-CPC. While the introduced OFGs in O-d-CPC increased current density, the potential range where high $H_2O_2$ selectivity is maintained tends to be narrower. In contrast, Co/d-CPC slightly reduced the disk current density while enhancing the ring current, thereby increasing the 2e$^-$ ORR selectivity. Additionally, the onset potential for the ORR reaction was improved due to the introduction of cobalt, which served as the active site. The onset potential was determined from the *I-V* curve obtained from the RRDE analysis, defined as the voltage at which the current density reaches 0.01 mA cm$^{-2}$. Co/O-d-CPC, which incorporates both new oxygen functional groups and the cobalt active sites, exhibits synergetic catalytic improvements. Therefore, the Co/O-d-CPC yielded superior performance in terms of current density and onset potential compared to d-CPC, with $H_2O_2$ selectivity maintained at approximately 93% between 0.2 and 0.45 V vs. RHE. Fig. 4g compares the onset potential and $H_2O_2$ selectivity of Co/O-d-CPC with other carbon-based and single-atom catalysts reported in previous studies, conducted in 0.1 M $K_2SO_4$.

As shown in Fig. 4c and f, under acidic conditions, Co/O-d-CPC also exhibited significantly higher current density and $H_2O_2$ selectivity compared to d-CPC. The 2e$^-$ ORR performance of carbon-based catalysts is typically limited by high overpotentials and low $H_2O_2$ selectivity under acidic conditions. However, Co/O-d-CPC can simultaneously enhance both 2e$^-$ ORR activity and $H_2O_2$ selectivity in an acidic condition. The superior performance of Co/O-d-CPC compared with other carbon-based and single-atom electrocatalysts reported in previous studies is further demonstrated (Tables S7–S9). Also, to compare the 2e$^-$ ORR performance of Co/O-d-CPC with other catalysts under a broad pH range, selectivity, onset potential, and maximum current density were employed as performance indicators (Figs. S36–S38). It is noteworthy that the superior performance is evident under all three electrolyte conditions, highlighting the versatility and effectiveness of Co/O-d-CPC in various pH environments. This performance of Co/O-d-CPC reinforces its potential as an effective catalyst.

To further elucidate the reaction kinetics, Tafel slopes were evaluated (Fig. 4h). Co/O-d-CPC exhibited the lowest Tafel slope of 66.88 mV dec$^{-1}$ under neutral conditions, outperforming Co/d-CPC (82.35 mV dec$^{-1}$), O-d-CPC (82.41 mV dec$^{-1}$), and d-CPC (94.27 mV dec$^{-1}$), indicating it offers the fastest ORR kinetics. This trend was consistently observed in both alkaline and acidic conditions (Fig. S39). Furthermore, Co/O-d-CPC demonstrated the lowest number of electron transfers across all three electrolytes (Figs. 4i and S40).

#### 3.4.2. Mass $H_2O_2$ electrosynthesis by H-type cell and flow cell test

The electrocatalytic performance of the Co/O-d-CPC catalyst was assessed using a two-chamber H-cell system. The H-type cell test was conducted in a 0.1 M $K_2SO_4$ electrolyte under a constant applied potential of 0.3 V vs. RHE. A calibration curve for $Ce(SO_4)_2$ concentrations ranging from 0 to 0.5 mM was utilized to quantify the $H_2O_2$ production and determine the Faradaic efficiency (Fig. S41). The results indicate stable current densities between 3.5 and 4.5 mA, demonstrating consistent $H_2O_2$ generation (Fig. S42). Notably, Co/O-d-CPC achieved a remarkable average $H_2O_2$ production rate of 619.95 mmol $g_{cat}^{-1}$ h$^{-1}$,

underscoring its exceptional catalytic performance over a 12-h period, with a Faradaic efficiency of approximately 90.5% (Fig. S43).

The mass production of $H_2O_2$ can be efficiently achieved in high current density-based electrochemical flow cell setups, utilizing an aerophilic gas diffusion layer made from hydrophobic-coated carbon fiber paper.[54] This design promotes rapid mass transfer of generated $H_2O_2$ while continuously supplying a large amount of $O_2$ gas, leading to efficient production. In this study, a variety of catalysts were tested for electrocatalytic $H_2O_2$ production in a reported custom-designed three-electrode flow cell (Fig. S44).[67] The production rate and Faradaic efficiency (FE) of $H_2O_2$ were measured under varying current densities (10–400 mA $cm^{-2}$), with iR compensation applied, across different pH conditions to evaluate the catalytic performance.

Co/O-d-CPC demonstrated an average FE of approximately 90% across the entire potential range in both alkaline and neutral electrolytes, outperforming Co/d-CPC and O/d-CPC by 7% to 10%, consistent with the results of the ring-disc electrode (RRDE) analysis (Fig. 5a and b). In the acidic electrolyte, the FE of Co/O-d-CPC decreased slightly to 80%, mainly due to the less favorable outer-sphere mechanism for $O_2$ adsorption on the catalyst surface. Consequently, a higher energy input is required for the oxygen reduction reaction (ORR) in acidic media.[68] Additionally, the lower energy barrier for breaking the O–OH bond in the acidic environment favors the formation of $H_2O$ over $H_2O_2$, further reducing both the ORR efficiency and the selectivity for $H_2O_2$.[69] Despite these challenges, Co/O-d-CPC still exhibited superior performance, maintaining a 16% to 20% higher FE in the acidic electrolyte compared to the other two catalysts (Co/d-CPC and O/d-CPC). These findings underscore the superior electrocatalytic properties of Co/O-d-CPC as a $2e^-$ ORR catalyst, achieving high $H_2O_2$ production rates across various pH conditions (Fig. 5a–c). Notably, as shown in Fig. 5b (Table S10), Co/O-d-CPC demonstrated excellent performance in the neutral electrolyte, with an $H_2O_2$ production rate of 14.4 mol $g^{-1}$ $h^{-1}$ achieved under an applied constant current density of 300 mA $cm^{-2}$, outperforming many extensively reported catalysts across a wide range of current densities (Fig. 5d). The stability of the optimal catalyst was also evaluated over a 30-h testing period, where it maintained over 80% FE (Fig. 5e) at an applied current density of 100 mA $cm^{-2}$ in 1 M $Na_2SO_4$. This performance is relatively superior to that of various reported catalysts operating under neutral conditions, particularly when considering the combined metrics of operational duration, current density, and Faradaic efficiency toward $H_2O_2$ production (Table S11).

To further evaluate the durability of the Co/O-d-CPC made cathodic

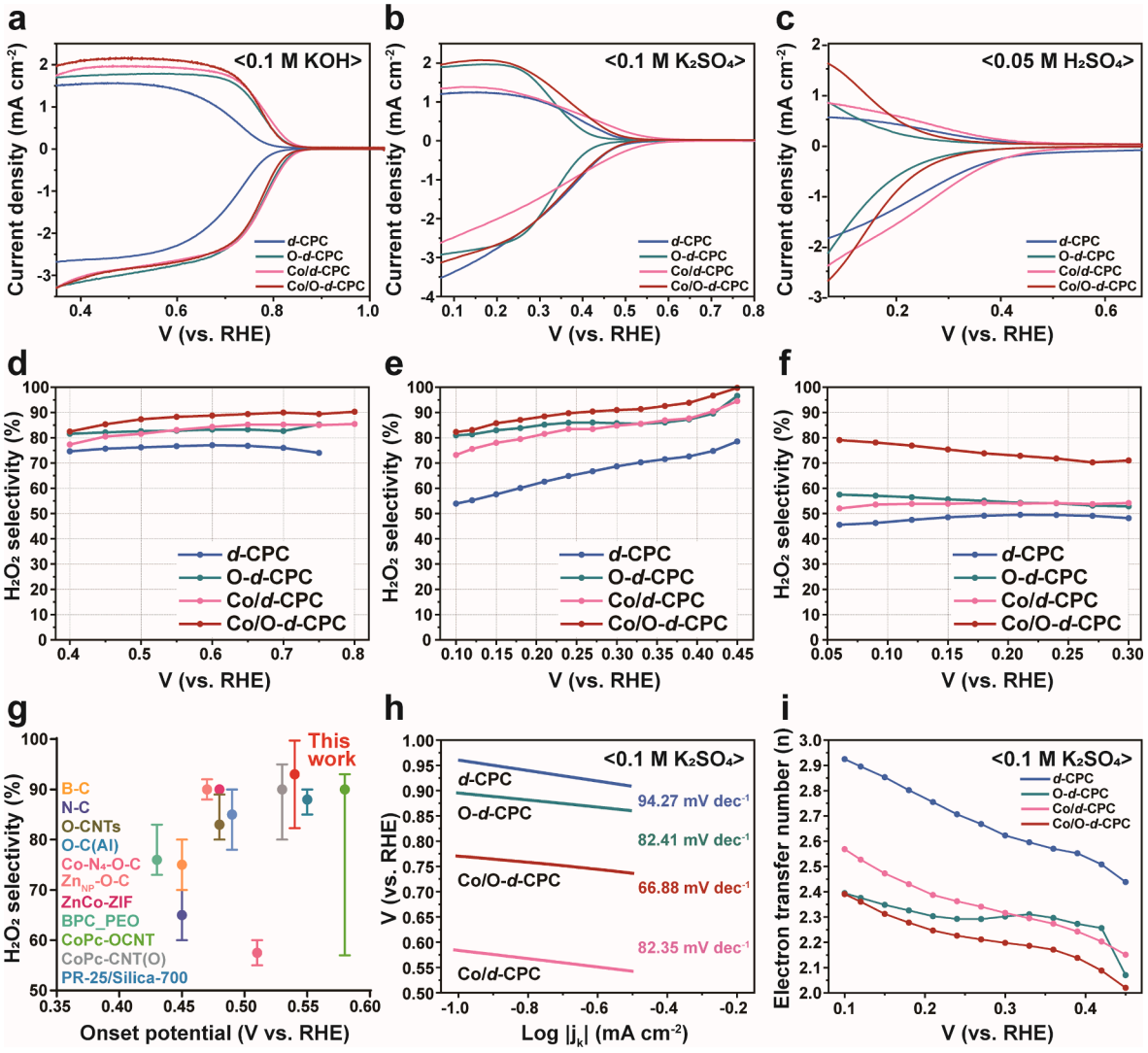


**Fig. 4.** Comparison of ORR performance. Polarization curves at 1600 rpm RRDE test in of d-CPC, O-d-CPC, Co/d-CPC, and Co/O-d-CPC in (a) 0.1 M KOH, (b) 0.1 M $K_2SO_4$ and (c) 0.05 M $H_2SO_4$. $H_2O_2$ selectivity of four materials in (d) 0.1 M KOH, (e) 0.1 M $K_2SO_4$ and (f) 0.05 M $H_2SO_4$. (g) Comparison of onset potential and $H_2O_2$ selectivity between Co/O-d-CPC and other carbon-based and single-atom catalysts reported in the literature under neutral electrolyte.[3,4,6,59–66] (h) Tafel plots of four materials and (i) electron transfer number of four materials in 0.1 M $K_2SO_4$.

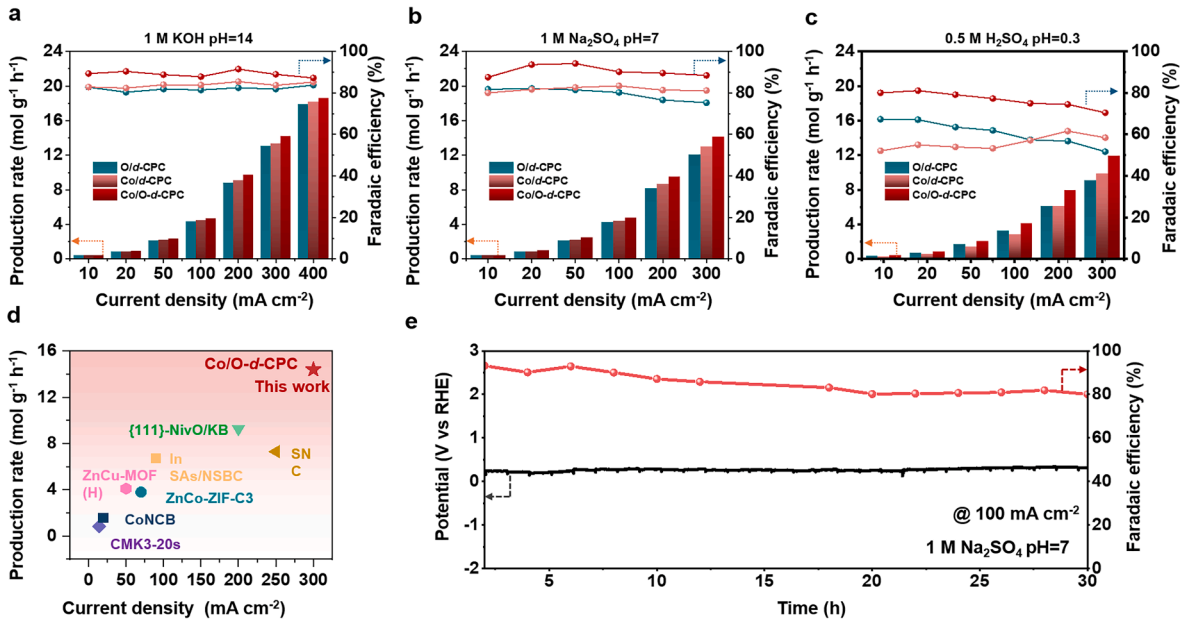


**Fig. 5.** $H_2O_2$ production performance was measured using a flow cell. (a) Faradaic efficiency and $H_2O_2$ production at different current densities in 1 M KOH (pH 14). (b) Faradaic efficiency and $H_2O_2$ production rate at varying current densities in 1 M $Na_2SO_4$ (pH 7). (c) Faradaic efficiency and $H_2O_2$ production rate at different current densities in 0.5 M $H_2SO_4$ (pH 0.3). (d) Comparison of $H_2O_2$ production rate with other works.[62,70–75] (e) Stability test of the Co/O-d-CPC catalyst at 100 mA $cm^{-2}$ in 1 M $Na_2SO_4$ for 30 h.

electrode, comprehensive structural characterizations were conducted. The characteristic XRD diffraction peaks at 18.3° and 26.8° (Fig. S45a), together with the D and G bands in the Raman spectra located at 1348 and 1591 $cm^{-1}$ (Fig. S45b), respectively, show no discernible changes before and after the 30-h stability test conducted at 100 mA $cm^{-2}$. These results indicate that the overall crystalline structure of the carbon matrix in Co/O-d-CPC is well preserved during prolonged electrochemical operation. This conclusion is further supported by the Co 2p XPS spectra (Fig. S45c), in which the characteristic Co $2p_{3/2}$ and Co $2p_{1/2}$ peaks at 781.6 and 796.5 eV, respectively, remain intact. Only a slight decrease in the Co atomic concentration is observed, from 1.9 at% to 1.6 at% after the stability test. Overall, these results suggest that no appreciable structural damage or phase transformation occurs under the applied operating conditions, demonstrating that the electrode assembled with a GDL exhibits good chemical and structural stability at 100 mA $cm^{-2}$. This highlights the promising durability of Co/O-d-CPC as a high-performance $2e^-$ ORR electrocatalyst for scalable $H_2O_2$ production.

## 4. Conclusion

The Co/O-d-CPC electrocatalyst investigated in this study has demonstrated exceptional catalytic performance for the $2e^-$ ORR across a wide pH range of electrolytes. This catalyst features cobalt phthalocyanine (CoPc) molecules with a Co-$N_4$ structure anchored onto oxygen-functionalized $CO_2$-derived porous carbon, to provide a synergistic effect between the oxygen functional groups and cobalt single atoms. Additionally, the defective mesoporous carbon structure plays a crucial role in providing sites for oxygen functional groups, which are likely located near defective regions, enhancing their interaction with Co single atoms. DFT simulations reveal that the $O_C$ group enhanced the activity of single cobalt active sites, interacting favorably with Co-SACs to stabilize the Co center. This stabilization weakens the adsorption energy of OOH ($E_{*OOH}$) by reducing the strong coupling between Co and the OOH intermediate, leading to improved catalytic performance. The catalyst exhibits high $H_2O_2$ selectivity in neutral, alkaline, and acidic electrolytes, with approximately 93% selectivity at 0.3 V vs. RHE in neutral conditions. In flow cell experiments, Co/O-d-CPC demonstrated high $H_2O_2$ selectivity and production rates across various electrolyte conditions, consistent with RRDE results. Notably, under a neutral electrolyte, it achieved an outstanding $H_2O_2$ production rate of 14.4 mol $g^{-1}$ $h^{-1}$ at a constant current of 300 mA $cm^{-2}$, surpassing numerous widely studied catalysts across a broad range of current densities. Also, Co/O-d-CPC exhibited a high production rate of 619.95 mmol $g_{cat}^{-1}$ $h^{-1}$ in the H-cell test. These findings establish Co/O-d-CPC as an efficient and stable catalyst for $H_2O_2$ production, with significant potential for energy conversion and environmental remediation applications.

## CRediT authorship contribution statement

**Jimin Lee:** Writing – review & editing, Writing – original draft, Investigation, Formal analysis, Data curation, Conceptualization. **Yeongjun Yoon:** Writing – review & editing, Writing – original draft, Software, Investigation, Formal analysis, Data curation. **Wenjun Zhang:** Writing – review & editing, Writing – original draft, Investigation, Formal analysis, Data curation. **Won Chan Yun:** Writing – review & editing, Writing – original draft, Investigation, Formal analysis, Data curation. **Keun Hwa Chae:** Investigation, Formal analysis, Data curation. **Ayeong Byeon:** Supervision, Data curation. **Jinli Qiao:** Supervision, Resources. **Jong Min Kim:** Writing – review & editing, Supervision, Project administration. **Kyeounghak Kim:** Writing – review & editing, Supervision, Project administration, Funding acquisition. **Jae W. Lee:** Writing – review & editing, Supervision, Resources, Project administration, Investigation, Funding acquisition.

## Declaration of competing interest

Jinli Qiao is an Executive Editor for this journal and was not involved in the editorial review or the decision to publish this article. The authors declare that they have no known competing financial interests or personal relationships that could have appeared to influence the work reported in this paper.

## Acknowledgments

This work was supported by the Engineering Research Center (ERC),

funded by the National Research Foundation of Korea (RS-2022-NR070840). Also, this work was supported by the National Research Foundation of Korea grant funded by the Korean government (MSIT) (No. RS-2023-00209940).

## Appendix A. Supplementary data

Supplementary data to this article can be found online at https://doi.org/10.1016/j.matre.2026.100431.

## References


1. Siahrostami S, Verdaguer-Casadevall A, Karamad M, et al. Enabling direct $H_2O_2$ production through rational electrocatalyst design. *Nat Mater*. 2013;12(12):1137–1143.
2. Kim H, Lim TJ, Eom HH, Kim YJ, Kim K, Lee JW. Reconstructed fluorine doped perovskites for electrocatalytic urea production through reaction pathways with $CO_2$ and nitrate ions. *Appl Catal B Environ*. 2025;365:124974.
3. Zhang W, Choi JW, Kim S, et al. Penta nitrogen coordinated cobalt single atom catalysts with oxygenated carbon black for electrochemical $H_2O_2$ production. *Appl Catal B Environ*. 2023;331:122712.
4. Lee BH, Shin H, Rasouli AS, et al. Supramolecular tuning of supported metal phthalocyanine catalysts for hydrogen peroxide electrosynthesis. *Nat Catal*. 2023;6(3):234–243.
5. Byeon A, Yun WC, Kim JM, Lee JW. Non-precious metal catalysts for Two-Electron oxygen reduction reaction. *Chemelectrochem*. 2023;10(17):e202300234.
6. Lu Z, Chen G, Siahrostami S, et al. High-efficiency oxygen reduction to hydrogen peroxide catalysed by oxidized carbon materials. *Nat Catal*. 2018;1(2):156–162.
7. Chen S, Chen Z, Siahrostami S, et al. Designing boron nitride Islands in carbon materials for efficient electrochemical synthesis of hydrogen peroxide. *J Am Chem Soc*. 2018;140(25):7851–7859.
8. Byeon A, Choi JW, Lee HW, et al. $CO_2$-derived edge-boron-doped hierarchical porous carbon catalysts for highly effective electrochemical $H_2O_2$ production. *Appl Catal B Environ*. 2023;329:122557.
9. Yun WC, Byeon A, Lee JW. $CO_2$-Derived carbon materials for electrocatalysis: recent advances and future perspectives. *Energy Fuels*. 2025;39(37):17710–17729.
10. Jing L, Tian Q, Su P, et al. Mesoporous co–o–c nanosheets for electrochemical production of hydrogen peroxide in acidic medium. *J Mater Chem A*. 2022;10(8):4068–4075.
11. Dong K, Liang J, Wang Y, et al. Plasma-induced defective $TiO_2$-x with oxygen vacancies: a high-active and robust bifunctional catalyst toward $H_2O_2$ electrosynthesis. *Chem Catal*. 2021;1(7):1437–1448.
12. Zhang X, Xia Y, Xia C, Wang H. Insights into practical-scale electrochemical $H_2O_2$ synthesis. *Trends Chem*. 2020;2(10):942–953.
13. Liu W, Feng J, Yin R, et al. Tailoring oxygenated groups of monolithic cobalt-nitrogen-carbon frameworks for highly efficient hydrogen peroxide production in acidic media. *Chem Eng J*. 2022;430:132990.
14. Zhang J, Liu W, He F, et al. Highly dispersed Co atoms anchored in porous nitrogen-doped carbon for acidic $H_2O_2$ electrosynthesis. *Chem Eng J*. 2022;438:135619.
15. Ross RD, Sheng H, Ding Y, et al. Operando elucidation of electrocatalytic and redox mechanisms on a 2D metal organic framework catalyst for efficient electrosynthesis of hydrogen peroxide in neutral media. *J Am Chem Soc*. 2022;144(34):15845–15854.
16. Zhou Z, Pei Z, Wei L, Zhao S, Jian X, Chen Y. Electrocatalytic hydrogen evolution under neutral pH conditions: current understandings, recent advances, and future prospects. *Energy Environ Sci*. 2020;13(10):3185–3206.
17. Choi JW, Byeon A, Kim S, et al. Mesoporous boron-doped carbon with curved $B_4C$ active sites for highly efficient $H_2O_2$ electrosynthesis in neutral media and air-supplied environments. *Adv Mater*. 2025;37(9):2415712.
18. Jing L, Tian Q, Wang W, et al. Unveiling favorable microenvironment on porous doped carbon nanosheets for superior $H_2O_2$ electrosynthesis in neutral media. *Adv Energy Mater*. 2024;14(19):202304418.
19. Chen S, Luo T, Chen K, et al. Chemical identification of catalytically active sites on oxygen-doped carbon nanosheet to Decipher the high activity for electro-synthesis hydrogen peroxide. *Angew Chem Int Ed*. 2021;60(30):16607–16614.
20. Chen G, Liu J, Li Q, et al. A direct $H_2O_2$ production based on hollow porous carbon sphere-sulfur nanocrystal composites by confinement effect as oxygen reduction electrocatalysts. *Nano Res*. 2019;12(10):2614–2622.
21. Pang Y, Wang K, Xie H, Sun Y, Titirici MM, Chai GL. Mesoporous carbon hollow spheres as efficient electrocatalysts for oxygen reduction to hydrogen peroxide in neutral electrolytes. *ACS Catal*. 2020;10(14):7434–7442.
22. Byeon A, Yun WC, Kim JM, Lee JW. Recent progress in heteroatom-doped carbon electrocatalysts for the two-electron oxygen reduction reaction. *Chem Eng J*. 2023;456:141042.
23. Zhu J, Xiao X, Zheng K, et al. KOH-treated reduced graphene oxide: 100% selectivity for $H_2O_2$ electroproduction. *Carbon*. 2019;153:6–11.
24. Li B, Zhao C, Liu J, Zhang Q. Electrosynthesis of hydrogen peroxide synergistically catalyzed by Atomic co–nx–c sites and oxygen functional groups in noble-metal-free electrocatalysts. *Adv Mater*. 2019;31(35):1808173.
25. Han GF, Li F, Zou W, et al. Building and identifying highly active oxygenated groups in carbon materials for oxygen reduction to $H_2O_2$. *Nat Commun*. 2020;11(1):2209.
26. Wu Y, Yuan Q, Zhao Y, et al. Hydroxylated boron crystal domain-modulated heterostructure carbon catalysts for efficient hydrogen peroxide generation. *J Am Chem Soc*. 2025;147(29):25295–25305.
27. Zhang L, Jin N, Yang Y, et al. Advances on axial coordination design of single-atom catalysts for energy electrocatalysis: a review. *Nano-Micro Lett*. 2023;15(1):228.
28. Shim J, Lee J, Shin H, et al. Efficient $H_2O_2$ electrosynthesis in acidic media via Multiscale catalyst optimization. *Adv Mater*. 2025;37(17):2418489.
29. Tang C, Chen L, Li H, et al. Tailoring acidic oxygen reduction selectivity on single-atom catalysts via modification of first and second coordination spheres. *J Am Chem Soc*. 2021;143(20):7819–7827.
30. Gong H, Wei Z, Gong Z, et al. Low-Coordinated Co-N-C on oxygenated graphene for efficient electrocatalytic $H_2O_2$ production. *Adv Funct Mater*. 2022;32(5):2106886.
31. Zhao Q, Wang Y, Lai WH, et al. Approaching a high-rate and sustainable production of hydrogen peroxide: oxygen reduction on co–n–c single-atom electrocatalysts in simulated seawater. *Energy Environ Sci*. 2021;14(10):5444–5456.
32. Zhang Y, Chen D, Yu S, Feng Y, Zhang C, Hu J. Al-Induced local coordination engineering of Ni: steering the two-electron oxygen reduction process. *Adv Funct Mater*. 2025:e13626.
33. Zhang Y, Jiang H, Zhang C, et al. High-efficiency oxygen reduction by late transition metal oxides to produce $H_2O_2$. *J Mater Chem A Mater*. 2024;12(10):6123–6133.
34. Chen S, Luo T, Li X, et al. Identification of the highly active Co–$N_4$ coordination motif for selective oxygen reduction to hydrogen peroxide. *J Am Chem Soc*. 2022;144(32):14505–14516.
35. Kim YK, Park JH, Lee JW. Facile nano-templated $CO_2$ conversion into highly interconnected hierarchical porous carbon for high-performance supercapacitor electrodes. *Carbon*. 2018;126:215–224.
36. Park JH, Yang J, Kim D, Gim H, Choi WY, Lee JW. Review of recent technologies for transforming carbon dioxide to carbon materials. *Chem Eng J*. 2022;427:130980.
37. Kresse G, Furthmü J. Efficient iterative schemes for Ab initio total-energy calculations using a plane-wave basis set. *Phys Rev B*. 1996;54:11169.
38. Blochl PE. Projector Augmented-+rave method. *Phys Rev B*. 1994;50:17953–17979.
39. Perdew JP, Burke K, Ernzerhof M. Generalized gradient approximation made simple. *Phys Rev Lett*. 1996;77:3865.
40. Caldeweyher E, Mewes JM, Ehlert S, Grimme S. Extension and evaluation of the $D_4$ London-dispersion model for periodic systems. *Phys Chem Chem Phys*. 2020;22(16):8499–8512.
41. Mathew K, Kolluru VSC, Mula S, Steinmann SN, Hennig RG. Implicit self-consistent electrolyte model in plane-wave density-functional theory. *J Chem Phys*. 2019;151(23):234101.
42. Jiao Y, Zheng Y, Jaroniec M, Qiao SZ. Design of electrocatalysts for oxygen- and hydrogen-involving energy conversion reactions. *Chem Soc Rev*. 2015;44(8):2060–2086.
43. Tang W, Sanville E, Henkelman G. A grid-based Bader analysis algorithm without lattice bias. *Condense Matter*. 2009;21(8):084204.
44. Sanville E, Kenny SD, Smith R, Henkelman G. Improved grid-based algorithm for Bader charge allocation. *J Comput Chem*. 2007;28(5):899–908.
45. Henkelman G, Arnaldsson A, Jónsson H. A fast and robust algorithm for Bader decomposition of charge density. *Comput Mater Sci*. 2006;36(3):354–360.
46. Yu M, Trinkle DR. Accurate and efficient algorithm for Bader charge integration. *J Chem Phys*. 2011;134(6):064111.
47. Nelson R, Ertural C, George J, Deringer VL, Hautier G, Dronskowski R. LOBSTER: local orbital projections, atomic charges, and chemical-bonding analysis from projector-augmented-wave-based density-functional theory. *J Comput Chem*. 2020;41(21):1931–1940.
48. Hwang B, Yang J, Kim D, Yun WC, Lee JW. Redox enhanced membraneless electrochemical capacitor with $CO_2$-derived hierarchical porous carbon electrodes. *Electrochim Acta*. 2023;442:141871.
49. Lee D, Yang J, Yun WC, Lee JW. Nitrogen-doped hierarchical porous carbon derived from $CO_2$ for the high-performance cathode of lithium-sulfur battery. *Electrochim Acta*. 2025;520:145867.
50. Zhang J, Lee JW. Production of boron-doped porous carbon by the reaction of carbon dioxide with sodium borohydride at atmospheric pressure. *Carbon*. 2013;53:216–221.
51. Qin M, Fan S, Wang L, et al. Oxygen and nitrogen co-doped ordered mesoporous carbon materials enhanced the electrochemical selectivity of $O_2$ reduction to $H_2O_2$. *J Colloid Interface Sci*. 2020;562:540–549.
52. Huo L, Liu B, Zhang G, Si R, Liu J, Zhang J. 2D Layered non-precious metal mesoporous electrocatalysts for enhanced oxygen reduction reaction. *J Mater Chem A*. 2017;5(10):4868–4878.
53. Tian Y, Deng D, Xu L, et al. Strategies for sustainable production of hydrogen peroxide via oxygen reduction reaction: from catalyst design to device setup. *Nano-Micro Lett*. 2023;15(1):122.
54. Hofer C, Skákalová V, Görlich T, et al. Direct imaging of light-element impurities in graphene reveals triple-coordinated oxygen. *Nat Commun*. 2019;10(1):4570.
55. Yu A, Liu S, Yang Y. Recent advances in electrosynthesis of $H_2O_2$ *via* two-electron oxygen reduction reaction. *Chem Commun*. 2024;60(40):5232–5244.
56. Xia D, Yang X, Xie L, et al. Direct growth of carbon nanotubes doped with single Atomic Fe–$N_4$ active sites and neighboring graphitic nitrogen for efficient and stable oxygen reduction electrocatalysis. *Adv Funct Mater*. 2019;29(49):1906174.
57. Wang Y, Meng P, Yang Z, et al. Regulation of atomic fe-spin State by crystal field and magnetic field for enhanced oxygen electrocatalysis in rechargeable Zinc-Air batteries. *Angew Chem Int Ed*. 2023;62(28):e202304229.
58. Liu S, Li Z, Wang C, et al. Turning main-group element magnesium into a highly active electrocatalyst for oxygen reduction reaction. *Nat Commun*. 2020;11(1):938.

59. Yun WC, Yang J, Lee D, et al. Enhanced electroproduction of hydrogen peroxide with oxidized boron-doped carbon catalysts synthesized from gaseous $CO_2$. *J CO2 Util*. 2024;84:102833.
60. Huang B, Cui Y, Hu R, Huang J, Guan L. Promoting the two-electron oxygen reduction reaction performance of carbon nanospheres by pore engineering. *ACS Appl Energy Mater*. 2021;4(5):4620–4629.
61. Xia Y, Zhao X, Xia C, et al. Highly active and selective oxygen reduction to $H_2O_2$ on boron-doped carbon for high production rates. *Nat Commun*. 2021;12(1):4225.
62. Zhang C, Yuan L, Liu C, et al. Crystal engineering enables cobalt-based metal–organic frameworks as high-performance electrocatalysts for $H_2O_2$ production. *J Am Chem Soc*. 2023;145(14):7791–7799.
63. Zhang S, Xu W, He P, et al. Tafel analysis guided optimization of $Zn_{NP}$-O-C catalysts for the selective 2-Electron oxygen reduction reaction in neutral media. *J Phys Chem Lett*. 2022;13(15):3409–3416.
64. Cao P, Quan X, Nie X, et al. Metal single-site catalyst design for electrocatalytic production of hydrogen peroxide at industrial-relevant currents. *Nat Commun*. 2023;14(1):172.
65. Yang Q, Xu W, Gong S, et al. Atomically dispersed Lewis acid sites boost 2-electron oxygen reduction activity of carbon-based catalysts. *Nat Commun*. 2020;11(1).
66. Li Y, Cheng H, Wang M, Xu J, Guan L. Highly coordinative molecular cobalt-phthalocyanine electrocatalyst on an oxidized single-walled carbon nanotube for efficient hydrogen peroxide production. *Mater Horiz*. 2024;11(10):2517–2527.
67. Yin H, Pan R, Zou M, et al. Recent advances in carbon-based single-atom catalysts for electrochemical oxygen reduction to hydrogen peroxide in acidic media. *Nanomaterials*. 2024;14(10):835.
68. Steimecke M, Seiffarth G, Schneemann C, Oehler F, Förster S, Bron M. Higher-Valent nickel oxides with improved oxygen evolution activity and stability in alkaline media prepared by high-temperature treatment of $Ni(OH)_2$. *ACS Catal*. 2020;10(6):3595–3603.
69. Jung E, Shin H, Lee BH, et al. Atomic-level tuning of co–n–c catalyst for high-performance electrochemical $H_2O_2$ production. *Nat Mater*. 2020;19(4):436–442.
70. Zhang W, Le TT, Shin D, et al. Higher-valent nickel oxides with enhanced two-electron oxygen reduction in advanced electro-Fenton system for organic pollutants degradation. *Appl Catal B Environ*. 2025;361:124666.
71. Mou Z, Mu Y, Liu L, et al. In-Plane topological-defect-enriched graphene as an efficient metal-free catalyst for pH-Universal $H_2O_2$ electrosynthesis. *Small*. 2024;20(29):2400564.
72. Pei Z, Li Y, Fan G, et al. Low-Coordinated conductive ZnCu metal-organic frameworks for highly selective $H_2O_2$ electrosynthesis. *Small*. 2024;20:2403808.
73. Wang YL, Li SS, Yang XH, et al. One minute from pristine carbon to an electrocatalyst for hydrogen peroxide production. *J Mater Chem A*. 2019;7(37):21329–21337.
74. Zhang E, Tao L, An J, et al. Engineering the local atomic environments of indium Single-Atom catalysts for efficient electrochemical production of hydrogen peroxide. *Angew Chem Int Ed*. 2022;61(12):e202117347.
75. Liu L, Kang L, Feng J, et al. Atomically dispersed asymmetric cobalt electrocatalyst for efficient hydrogen peroxide production in neutral media. *Nat Commun*. 2024;15(1):4079.




**Jimin Lee** received her M.S. degree in Chemical and Biomolecular Engineering from Korea Advanced Institute of Science and Technology (KAIST). She is currently pursuing a Ph.D. in Materials Science and Engineering at Seoul National University. Her previous research focused on the two-electron oxygen reduction reaction ($2e^-$ ORR) using single-atom catalysts on carbon-based supports. She is currently focusing on electrochemical C-N coupling and nitrate reduction ($NO_3RR$). She also conducts research integrating experimental and machine learning approaches for catalyst design.



**Yeongjun Yoon** is currently pursuing an integrated Master's and Ph.D. degree in the Department of Chemical Engineering at Hanyang University, South Korea. His research focuses on advancing computational materials science and heterogeneous catalysis. Specifically, he utilizes Density Functional Theory (DFT) and molecular dynamics simulations combined with Machine Learning Interatomic Potentials (MLIP) to design and analyze novel functional materials. His current interests also extend to integrating artificial intelligence into the predictive modeling of material synthesizability and catalytic performance for sustainable energy applications.



**Wenjun Zhang** received her degree for developing non-noble two-electron oxygen reduction reaction ($2e^-$ ORR) electrocatalysts for $H_2O_2$ production and applying them to wastewater treatment. She pursued her Ph.D. at the KIST School, University of Science and Technology (UST), Korea, and obtained the degree in February 2025. Since March 2025, she has been working as a postdoctoral researcher at the same institution (KIST), focusing on advanced electrocatalyst materials and system development, continuing her doctoral research. Her current research interests include electrocatalyst design and environmental applications.



**Won Chan Yun** is a Ph.D. candidate at the Korea Advanced Institute of Science and Technology (KAIST). His research focuses on the development of electrochemical catalysts for the two-electron oxygen reduction reaction ($2e^-$ ORR). Specifically, his current work explores utilizing carbon-based materials derived from $CO_2$ conversion processes as advanced electrochemical catalysts. He is particularly interested in defect and coordination engineering to enhance the performance of heteroatom active sites in these carbon materials.



**Jong Min Kim** received his Ph.D. from the Korea Advanced Institute of Science and Technology (KAIST) and is currently a Principal Researcher at the Extreme Materials Research Center of the Korea Institute of Science and Technology (KIST). His research focuses on developing high-performance electrocatalysts and support materials for various catalytic reactions and applying them to practical high-current-density electrochemical devices. From a materials perspective, he is also actively engaged in developing nanofabrication processes to create precisely controlled 3D nanostructures and in applying these 3D nanostructures to a wide range of fields.



**Kyeounghak Kim** is currently an Assistant Professor in the Department of Chemical Engineering at Hanyang University, South Korea. He is an expert in density functional theory (DFT) calculations and computational materials science. His research focuses on the bottom-up design and discovery of novel materials, utilizing atomic-level insights to replace traditional trial-and-error methods. He is particularly interested in massive material screening to develop cost-effective, highly active, and durable materials for diverse chemical reactions. His ultimate goal is to accelerate the discovery and development of specialized functional materials for various industrial and energy applications.



**Jae W. Lee** is a Korea Advanced Institute of Science and Technology (KAIST) ICT Chair Professor of Chemical and Biomolecular Engineering and currently serves as the Dean of the College of Engineering. He received his Ph.D. from Carnegie Mellon University in 2000. He is an AIChE Fellow and a member of the Korean NAE. His research focuses on converting $CO_2$ into diverse carbon materials for electrochemical energy conversion and storage applications. Specifically, he explores novel synthesis routes and property-tailoring techniques designed to maximize the electrochemical performance of these $CO_2$-derived carbon materials.